Supporting Information

The role of surface oxygen chemisorption on impurity states and electron localization in *n*-Type PbTe: Ar-Protected Grinding as a Remedy for Tripling *ZT*

Yingfei Tang [a,b#], Keke Liu [a#], Wei Wei [c], Shujun Han [a], Qing Zhang [a], Lingxiao Yu [a,b], Yaqiong Zhong [a], Vladimir Khovaylo [d], Qingjie Zhang [a], Xianli Su [a*], Xinfeng Tang [a*]

[a] *State Key Laboratory of Advanced Technology for Materials Synthesis and Processing, Wuhan University of Technology, Wuhan 430070, China*

[b] *International School of Materials Science and Engineering, Wuhan University of Technology, Wuhan 430070, China*

[c] *Accelink Technologies Co. Ltd, Wuhan 430205, China*

[d] *University of Science and Technology MISIS, Moscow 119049, Russia.*

[#]***These authors contributed equally.***

[*]***Corresponding authors:***

Xianli Su (suxianli@whut.edu.cn), Xinfeng Tang (tangxf@whut.edu.cn).

Experiment and calculation

1. Synthesis. For $Pb_{1-x}Sb_xTe$ (x = 0-0.005) and $Pb_{1-x}Bi_xTe$ (x = 0-0.005) samples, high purity Pb rods (5N), Sb blocks (5N), Bi blocks (5N) and Te blocks (6N) were weighed according to the stoichiometric ratio of $Pb_{1-x}Sb_xTe$ (x = 0-0.005) and $Pb_{1-x}Bi_xTe$ (x = 0-0.005) and placed in quartz tubes. The vacuum-sealed quartz tubes were then placed in a melting furnace, which were slowly heated to 1273 K at the speed of 100 K/h, and held for 24 h, following with quickly quenched in supersaturated salt water. The quenched samples were then vacuum annealed at 873 K for 72 h. The obtained ingots were then hand-ground in air or in glovebox into fine powder and subjected to spark plasma sintering (SPS) under the pressure of 40 MPa and at around 823 K. The relative density of the sintered bulk samples is greater than 95%.

2. Structure characterization and microscopic topography. The phase composition of $Pb_{1-x}Sb_xTe$ (x = 0-0.005) and $Pb_{1-x}Bi_xTe$ (x = 0-0.005) samples was examined by X-ray Diffractometry (PANalytical Empyrean, Cu Kα). The working voltage of the electron gun is 40 kV, and the measuring step size is 0.0033 °. The microstructure was observed by Electron Probe Microanalysis (JEOL JXA-8230).

3. Thermoelectric properties measurement. The low-temperature Hall resistivity (ρ_{xy}) and longitudinal resistivity (ρ_{xx}) from 5 T to -5 T were measured in a physical property measurement system (PPMS-9, Quantum Design). The electrical conductivity σ and Seebeck coefficient S of various samples were measured by ZEM-3 (ULVAC) under helium atmosphere. The thermal conductivity was calculated by the equation $\kappa = DC_p\rho$, where the thermal diffusivity (D) of the material was obtained by laser flash (Netzsch LFA 457), the heat capacity (C_p) was calculated by the Dulong–Petit law, and the density (ρ) was determined by Archimedean method. The uncertainty of measurements in S, σ and κ was about ±5%.

4. DFT Calculations.

All density functional theory calculations were carried out by Vienna ab initio simulation package (VASP) encoded with the projected augmented-wave (PAW) method. We chose the generalized gradient approximation functionals of Perdew, Burke, and Ernzerhof (GGA–PBE) as exchange-correlation functionals. The cut-off energy of the plane-wave basis was set at 500 eV. We used the experimental lattice parameters and atomic coordinates as initial geometry inputs and relaxed them with strict convergence criteria of 10^{-6} eV and 0.01 eV $Å^{-1}$ for energy and forces in the self-

consistent calculation, respectively. The van der Waals interactions were considered using the DFT-D3 method for more accurate description of van der Waals interactions during gas adsorption.

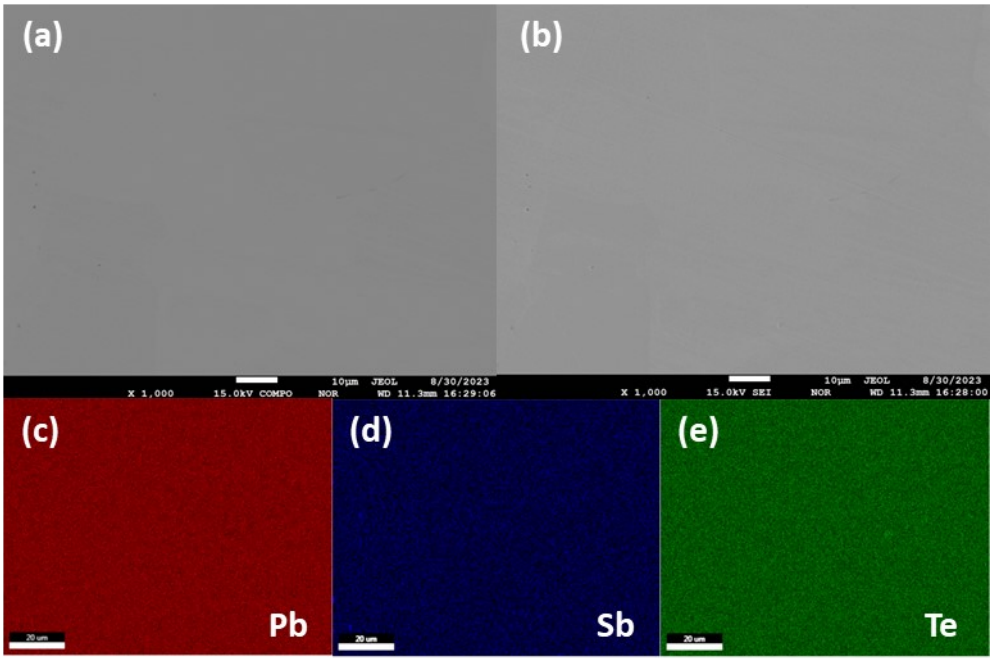

Figure S1. (a) Secondary electron image, (b) backscattered electron image and (c-e) corresponding elemental analysis for $Pb_{0.995}Sb_{0.005}Te$-air samples.

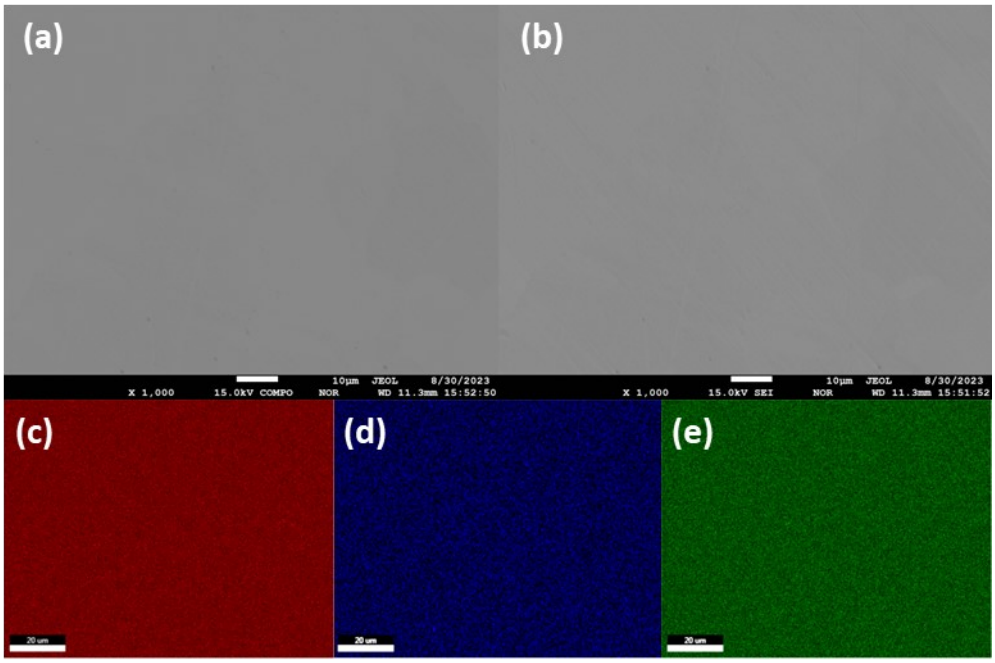

Figure S2. (a) Secondary electron image, (b) backscattered electron image and (c-e) corresponding elemental analysis for $Pb_{0.995}Sb_{0.005}Te$-Ar samples.

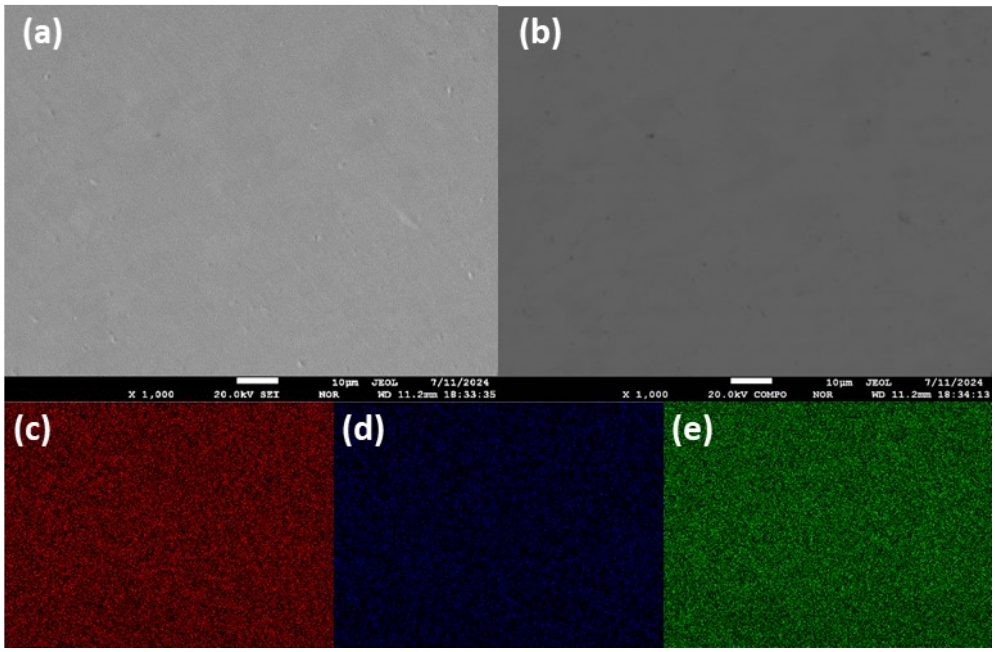

Figure S3. (a) Secondary electron image, (b) backscattered electron image and (c-e) corresponding elemental analysis for $Pb_{0.995}Bi_{0.005}Te$-air samples.

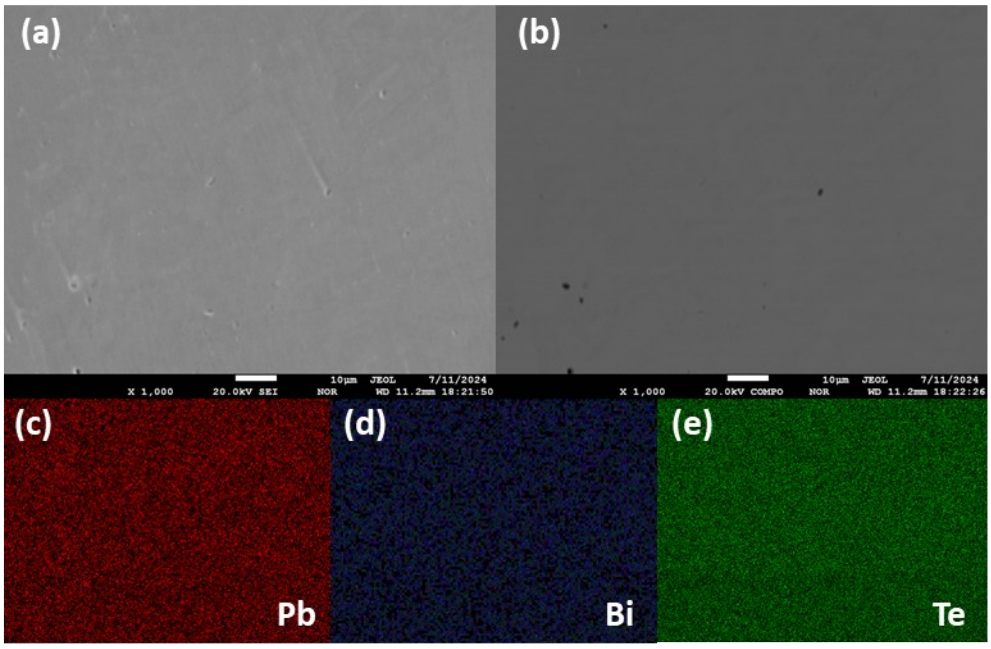

Figure S4. (a) Secondary electron image, (b) backscattered electron image and (c-e) corresponding elemental analysis for $Pb_{0.995}Bi_{0.005}Te$-Ar samples.

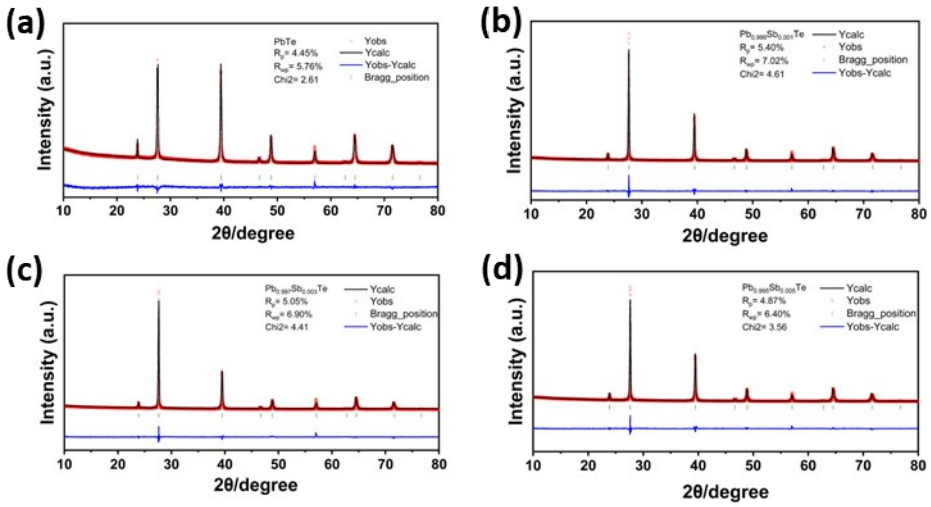

Figure S5. Refinement parameters for $Pb_{1-x}Sb_xTe$ (x = 0-0.005) samples.

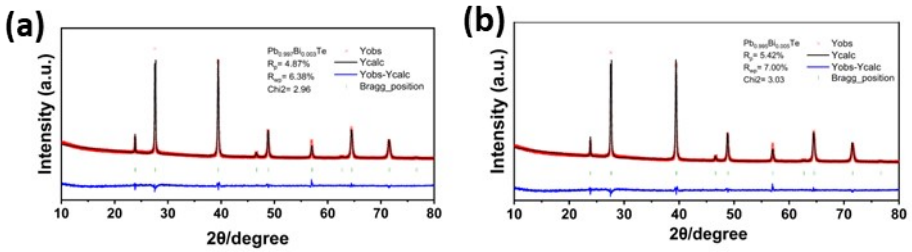

Figure S6. Refinement parameters for $Pb_{1-x}Bi_xTe$ (x = 0-0.005) samples.

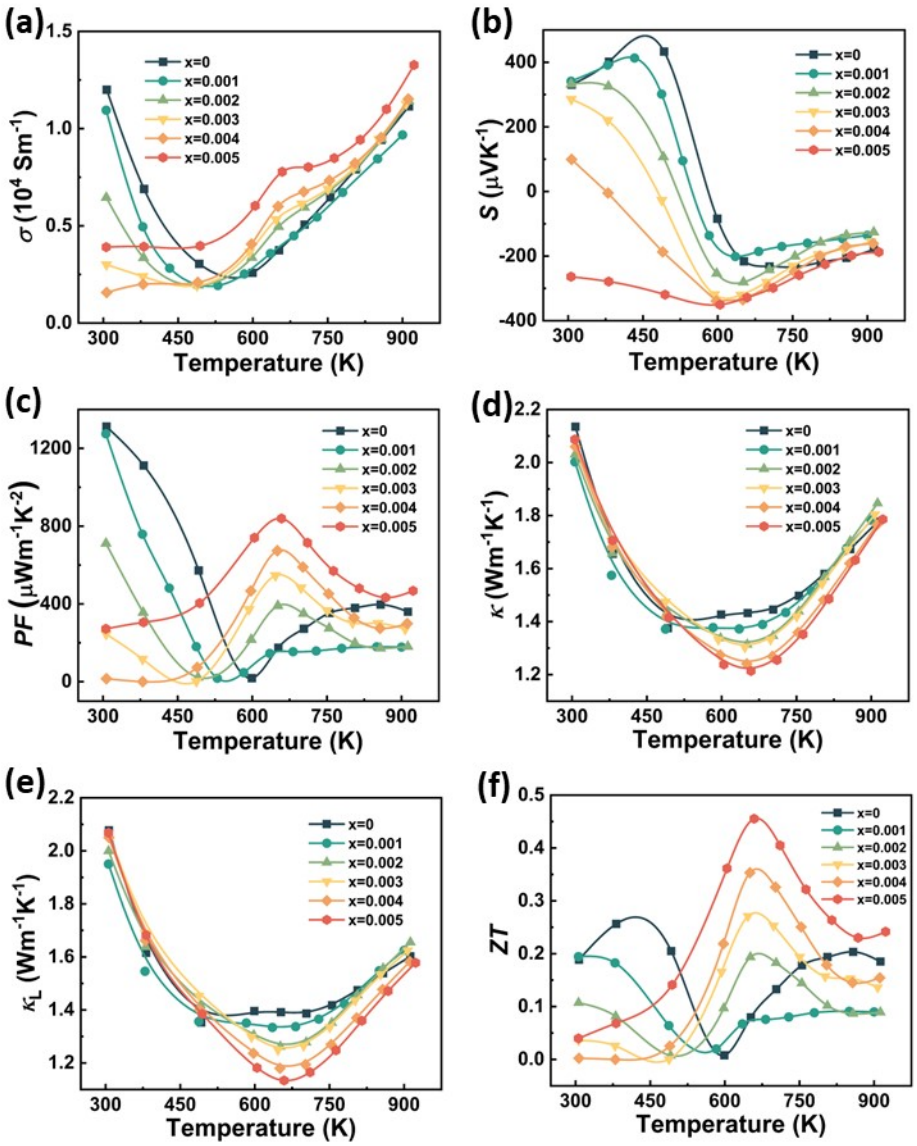

Figure S7. Temperature dependence of (a) Electrical conductivity, (b) Seebeck coefficient, (c) Power factor, (d) Thermoelectrical conductivity, (e) Lattice thermoelectrical conductivity, (f) Dimensionless figure of Merit *ZT* for $Pb_{1-x}Sb_xTe$-air (x = 0-0.005) samples.

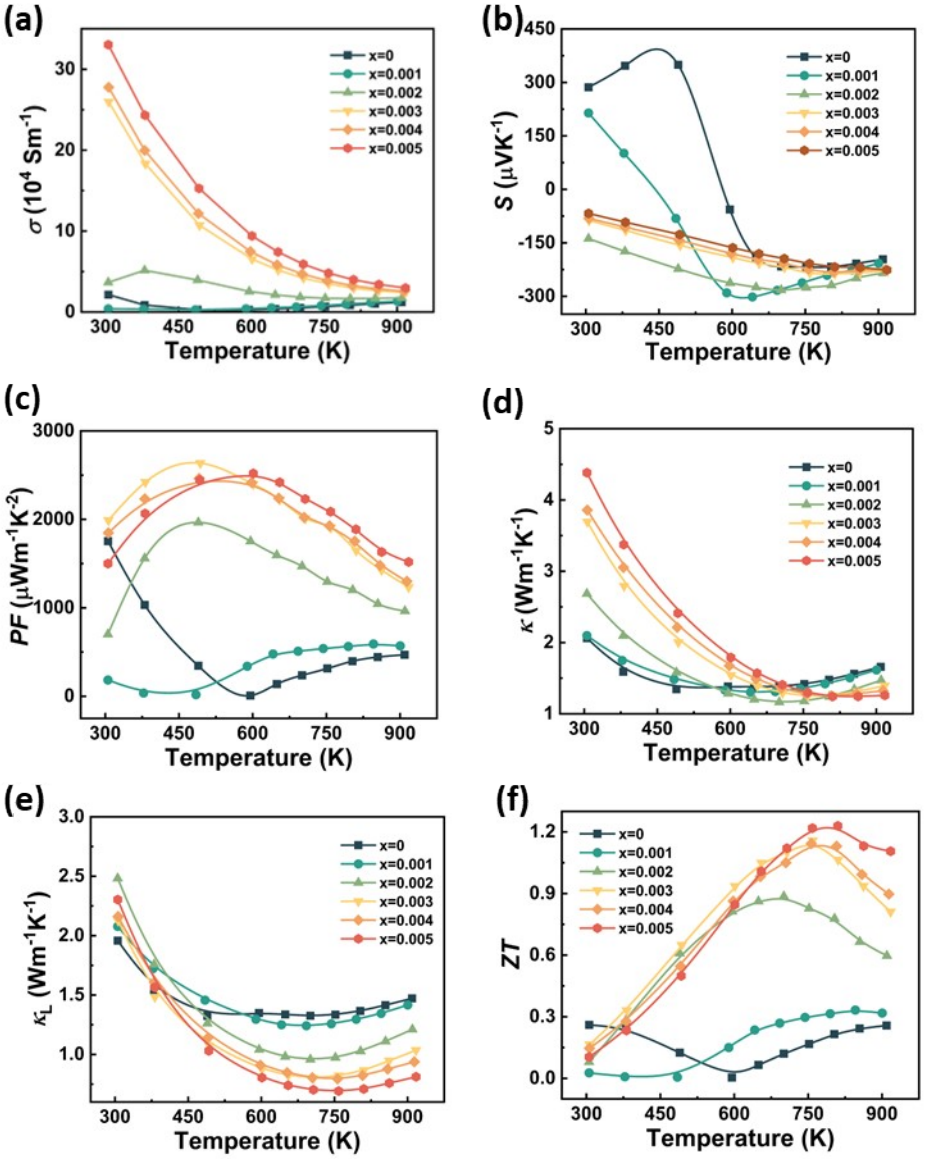

Figure S8. Temperature dependence of (a) Electrical conductivity, (b) Seebeck coefficient, (c) Power factor, (d) Thermoelectrical conductivity, (e) Lattice thermoelectrical conductivity, (f) Dimensionless figure of Merit *ZT* for $Pb_{1-x}Sb_xTe$-Ar (x = 0-0.005) samples.

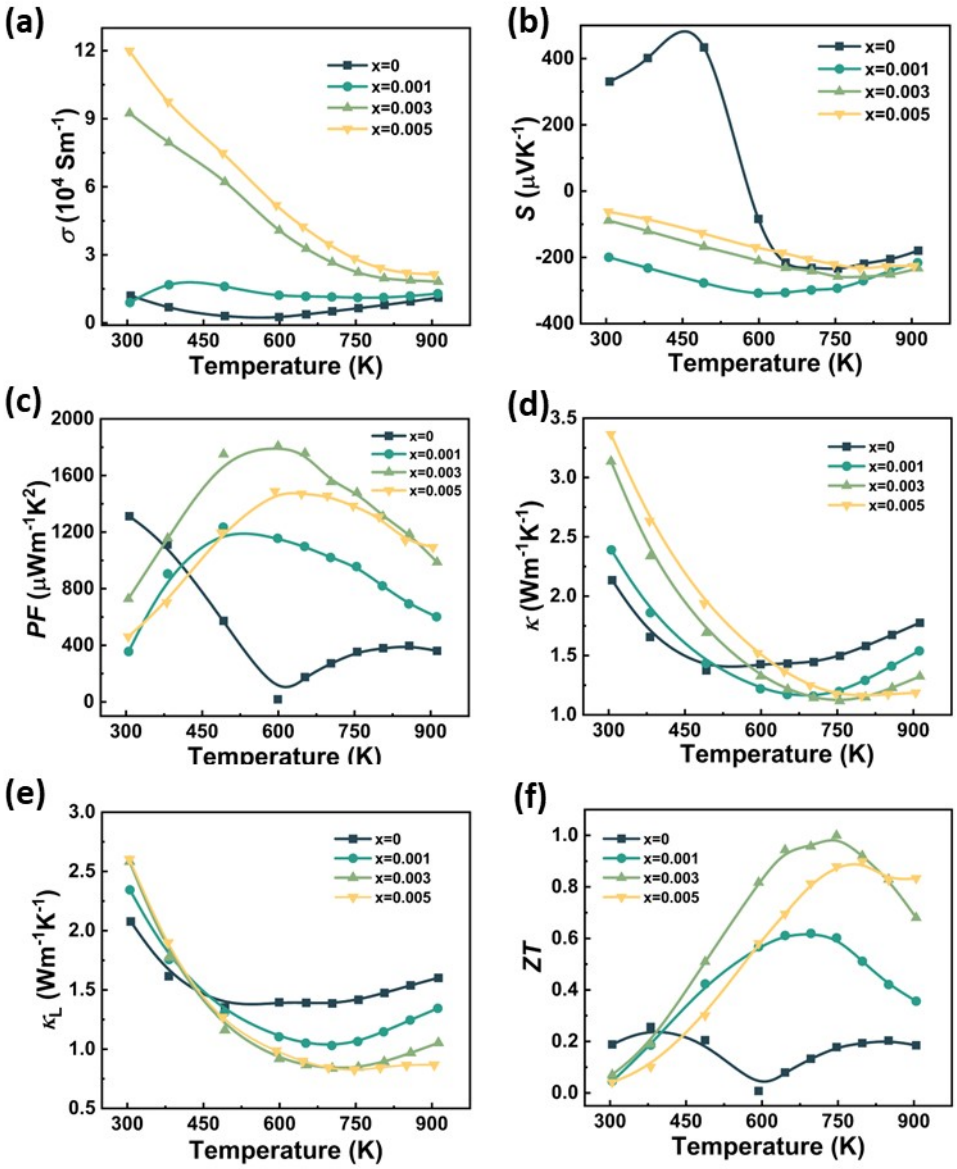

Figure S9. Temperature dependence of (a) Electrical conductivity, (b) Seebeck coefficient, (c) Power factor, (d) Thermoelectrical conductivity, (e) Lattice thermoelectrical conductivity, (f) Dimensionless figure of Merit *ZT* for $Pb_{1-x}Bi_xTe$-air (x = 0-0.005) samples.

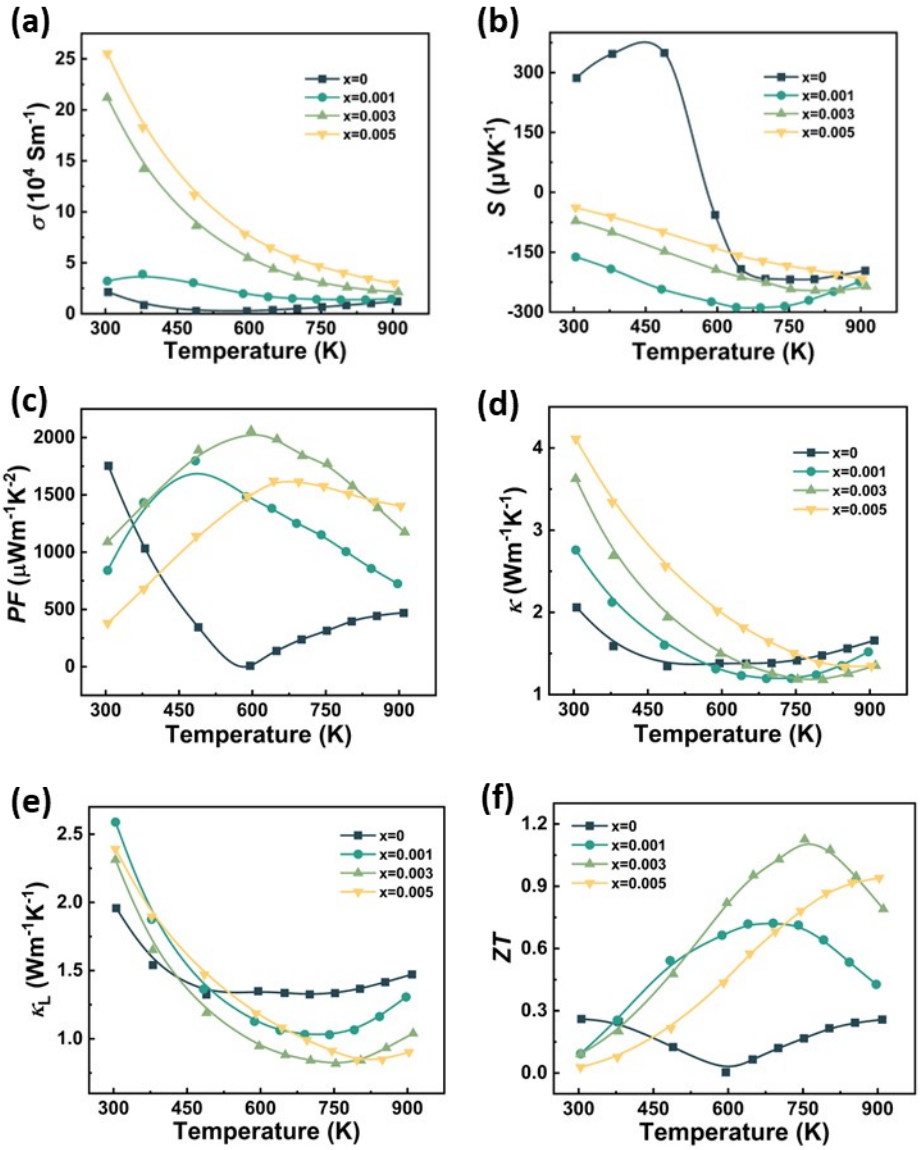

Figure S10. Temperature dependence of (a) Electrical conductivity, (b) Seebeck coefficient, (c) Power factor, (d) Thermoelectrical conductivity, (e) Lattice thermoelectrical conductivity, (f) Dimensionless figure of Merit *ZT* for $Pb_{1-x}Bi_xTe$-Ar (x = 0-0.005) samples.

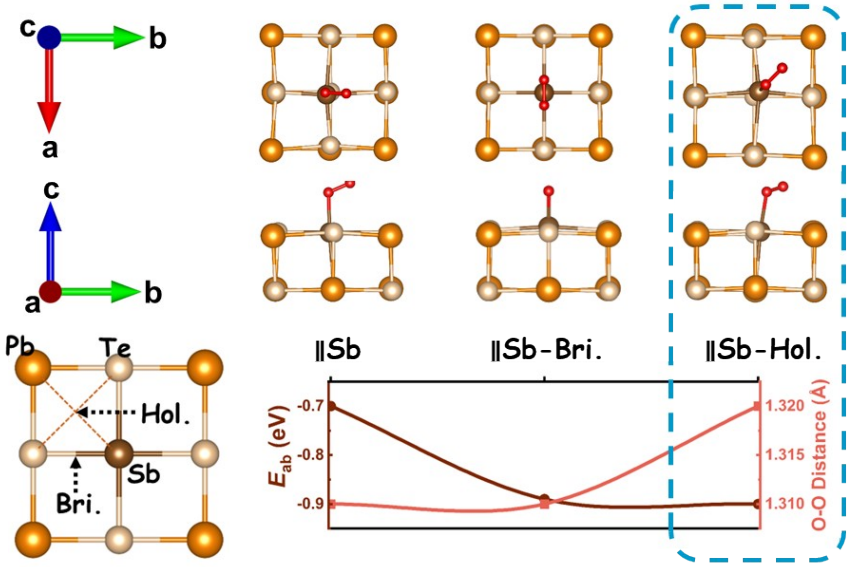

Figure S11. Possible adsorption configuration with calculated adsorption energies and O-O bond lengths of oxygen molecules at pristine cleaved surfaces for Sb -doped PbTe system.

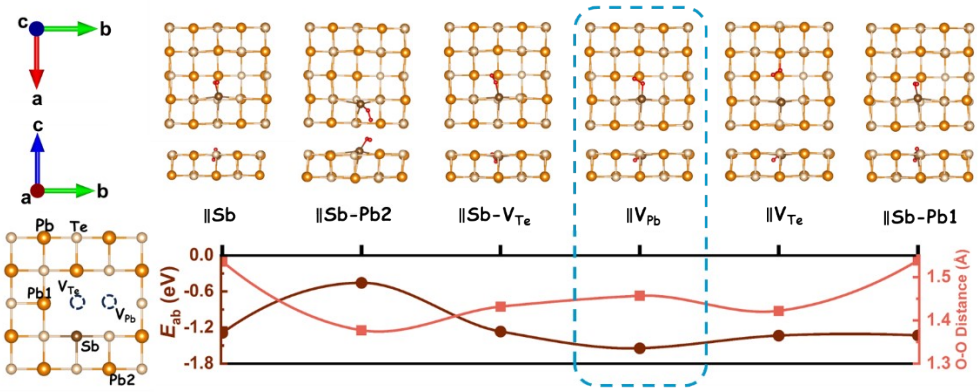

Figure S12. Possible adsorption configuration with calculated adsorption energies and O-O bond lengths of oxygen molecules at defective surfaces with (V_{Pb}+V_{Te}) vacancy pairs for Sb-doped PbTe system.

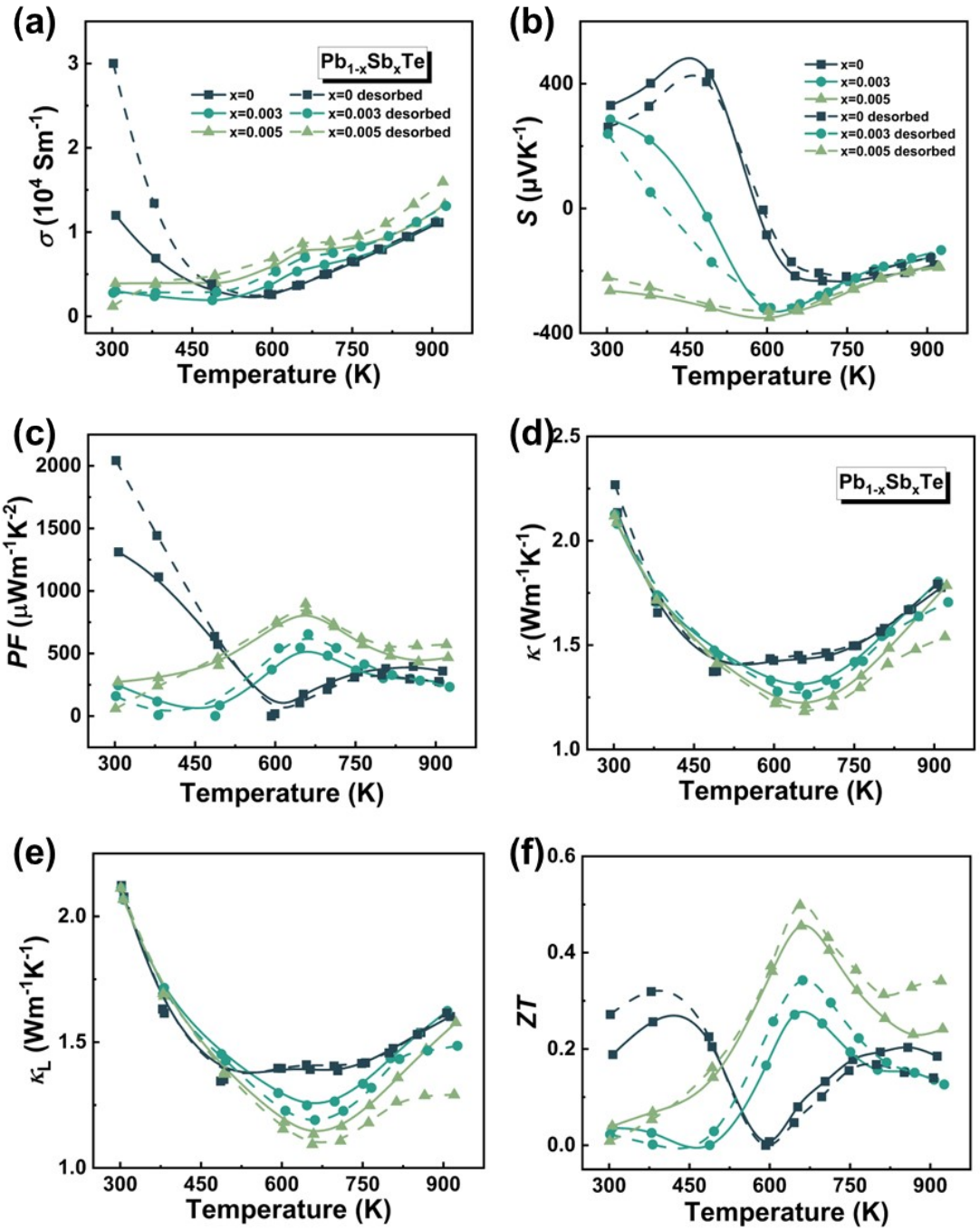

Figure S13 Comparison of (a) Electrical conductivity, (b) Seebeck coefficient, (c) Power factor, (d) Thermoelectrical conductivity, (e) Latticne thermoelectrical conductivity, (f) Dimensionless figure of Merit *ZT* between $Pb_{1-x}Sb_xTe$-air (x = 0-0.005) samples and desorbed $Pb_{1-x}Sb_xTe$-air (x = 0-0.005) samples.

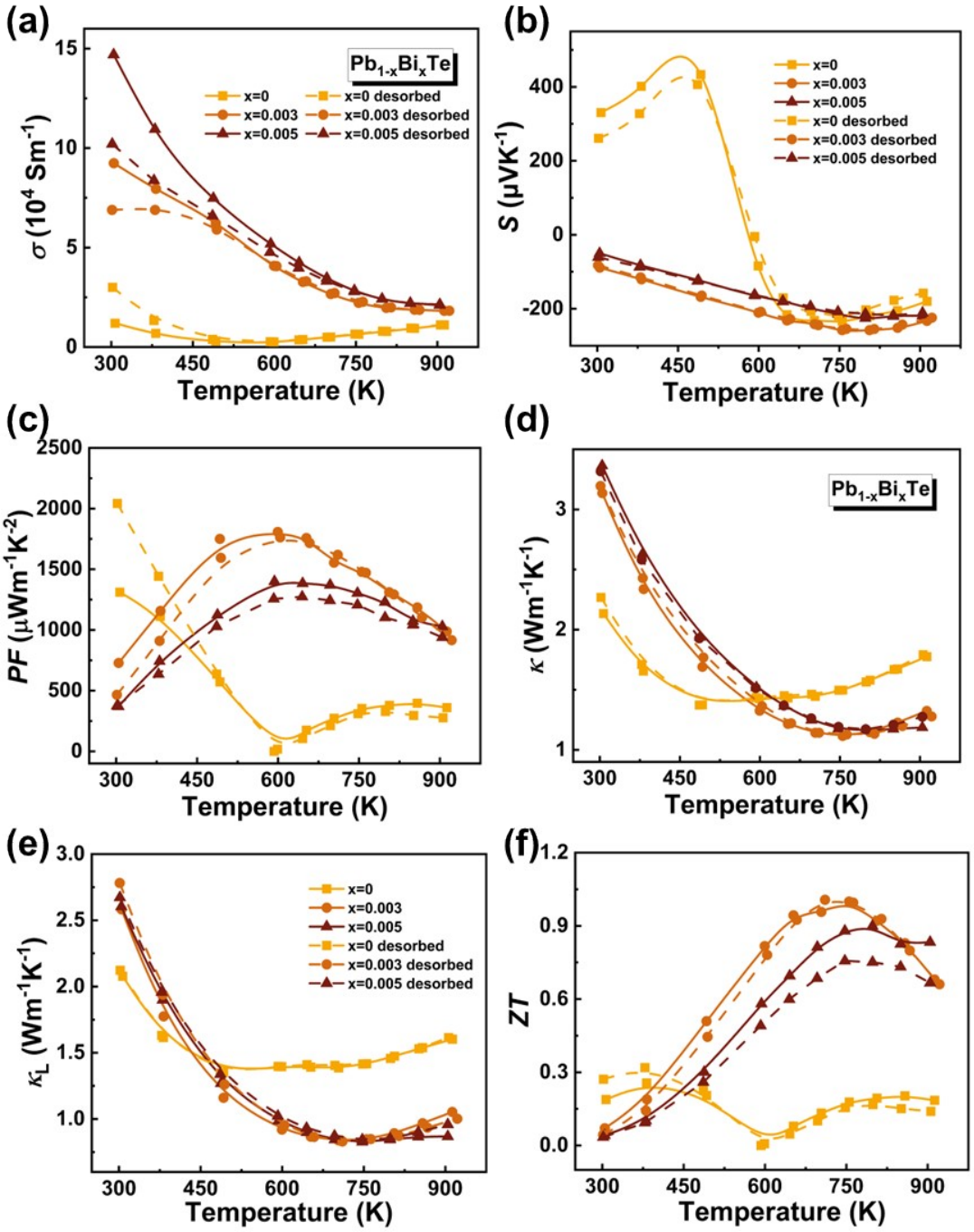

Figure S14. Comparison of (a) Electrical conductivity, (b) Seebeck coefficient, (c) Power factor, (d) Thermoelectrical conductivity, (e) Latticne thermoelectrical conductivity, (f) Dimensionless figure of Merit *ZT* between $Pb_{1-x}Sb_xTe$-air (x = 0-0.005) samples and desorbed $Pb_{1-x}Bi_xTe$-air (x = 0-0.005) samples.

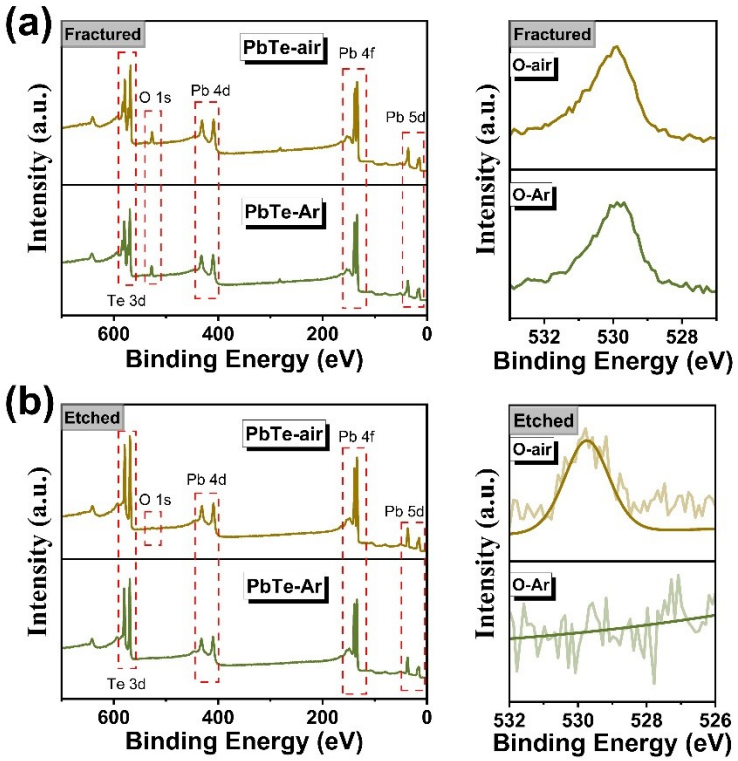

Figure S15. XPS spectra of the (a) freshly fractured and (b)Ar^{+}-etched PbTe surfaces.

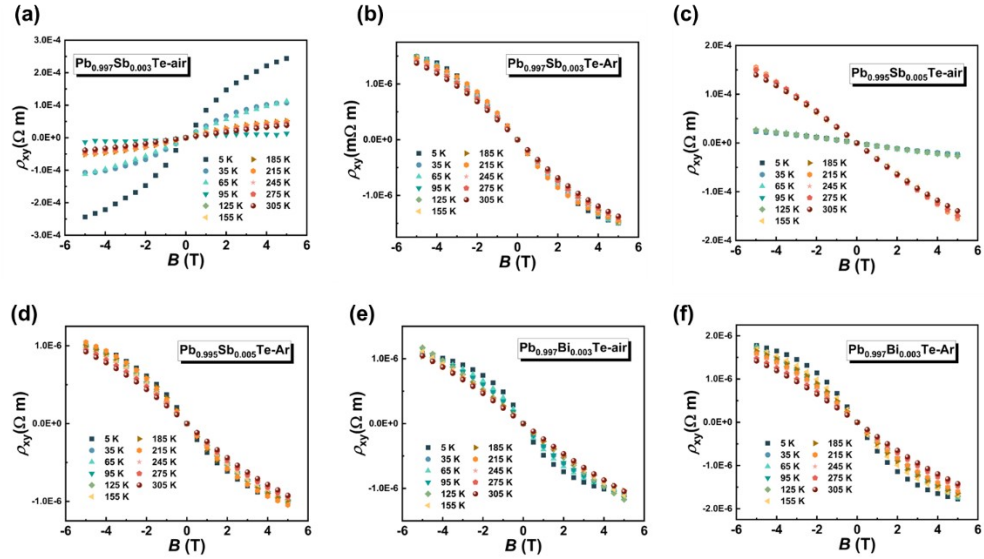

Figure S16. Hall resistivity as a function of magnetic field (B) of $Pb_{1-x}Sb_xTe$ (x = 0-0.005) samples and $Pb_{1-x}Bi_xTe$ (x = 0-0.003) samples in 5 K-305 K range.

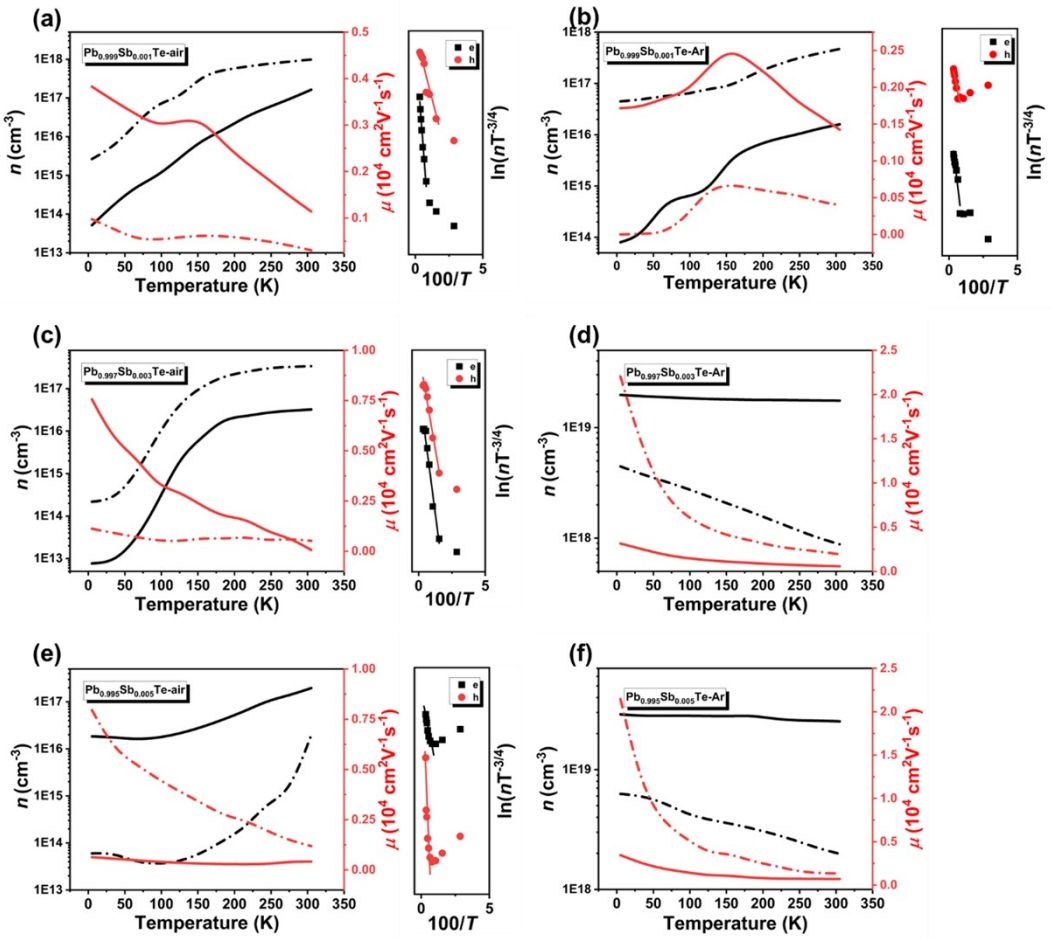

Figure S17. Calculated carrier density (n), carrier mobility (μ) and corresponding fitting process of impurity ionization energy for $Pb_{1-x}Sb_xTe$ (x = 0-0.005) samples.

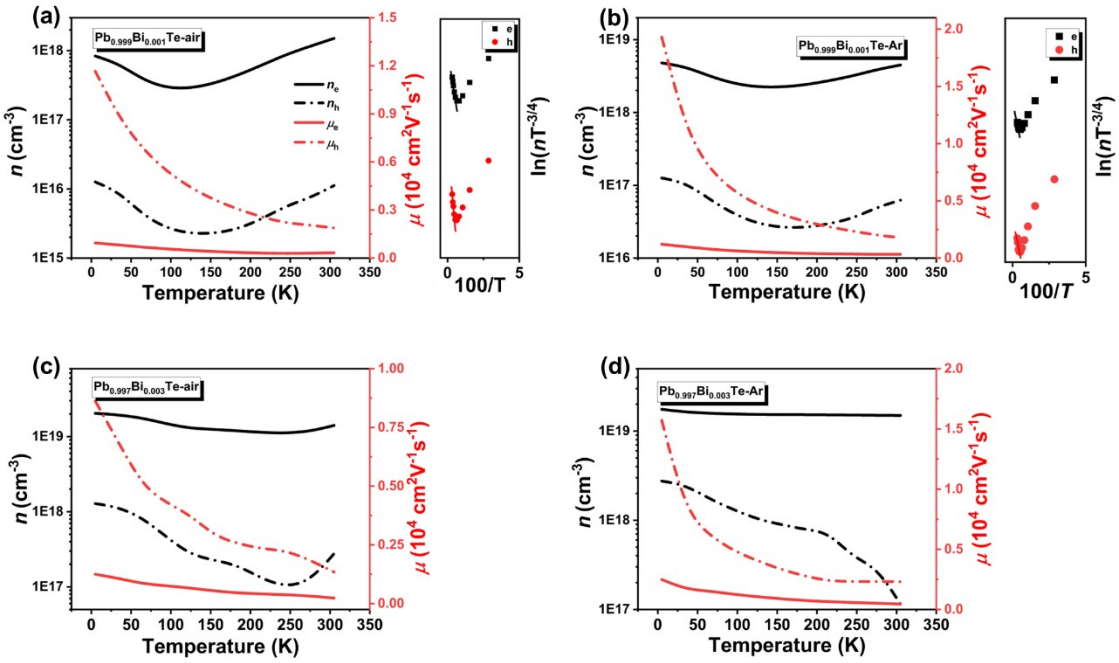

Figure S18. Calculated carrier density (n), carrier mobility (μ) and corresponding fitting process of impurity ionization energy for $Pb_{1-x}Bi_xTe$ (x = 0-0.003) samples.

Table S1. The density (ρ) of $Pb_{1-x}Sb_xTe$ (x=0.001-0.005) samples tested by Archimedes' principle.

Sample	x=0.001-air	x=0.003-air	x=0.005-air	x=0.001-Ar	x=0.003-Ar	x=0.005-Ar
ρ (g cm^{-3})	8.0399	7.9853	7.9769	7.9157	8.0364	8.0300

Table S2. The density (ρ) of $Pb_{1-x}Bi_xTe$ (x=0.001-0.005) samples tested by Archimedes' principle.

Sample	x=0.001-air	x=0.003-air	x=0.005-air	x=0.001-Ar	x=0.003-Ar	x=0.005-Ar
ρ (g cm^{-3})	8.1873	8.2648	8.2127	8.2104	8.2529	8.2155